

Research Papers

Mechanically induced thermal runaway severity analysis of Li-ion batteries and continuous energy release monitoring[☆]

L. Lin^a, K. Hartono^b, Y. Ko^c, R. Mallela^a, Y. Samantaray^c, H. Bouteiller^a, M.Z. Bazant^c, H. Wang^{a,*}

^a Material Science and Technology Division, Oak Ridge National Laboratory, Oak Ridge, TN 37831, USA

^b Vanderbilt University, Nashville, TN 37235, USA

^c Massachusetts Institute of Technology, Cambridge, MA 02139, USA

ARTICLE INFO

Keywords:

Li-ion battery
Thermal runaway
Mechanical abuse
Acoustic emission
IR imaging

ABSTRACT

The large-scale deployment of Li-ion batteries in stationary energy storage and electrical vehicle applications demands a strong focus on safety, particularly on the thermal runaway risk and severity evaluation. A standardized single-side mechanical indentation test protocol was developed to induce an internal short-circuit (ISC) and evaluate cells' thermal runaway severity at different state of charge (SOC). The observed hazard severity (OHS in five categories) and evaluated scores in this work have a comprehensive consideration of each cell's capacity, initial voltage, SOC, temperature and voltage change, allowing a better evaluation of the cells' thermal runaway potential. This method was applied to about 200 Li-ion batteries in order to build an extensive thermal runaway database covering various SOCs, capacities and chemistries. In this study, we monitored the transitions of stored electrochemical energy and applied mechanical energy into both thermal energy and acoustic emissions (AE). The surface temperature and mechanical failures were monitored by infrared imaging and AE to capture critical events within battery cells throughout the mechanical indentation tests. The initial temperature maps can predict two types of follow-up events: thermal runaway or gradual heat release via conduction. Analyzing each cell's severity, AEs, and leveraging the evolving database offer insights into predicting occurrences of thermal runaway. The test method, thermal runaway severity evaluation and prediction, and the corresponding database provide battery designers, manufacturers, and end-users a clear overview of Li-ion batteries' thermal runaway potential under mechanical abuse, advancing the safety design of Li-ion batteries.

1. Introduction

Li-ion batteries (LIBs) have been assimilated into everyday life through digital devices, power tools, stationary energy storage and electric vehicles since the early 1990s after Sony succeeded in the development and commercialization of LIB in 1991 [1]. LIBs have become essential for meeting the demands of low-cost, high-energy-density energy sources, but their safety remains a significant challenge in their utilization. One of the primary safety concerns is thermal runaway—a series of self-sustaining reactions triggered by internal failures that result in rapid heating, gas generation, and potentially catastrophic

outcomes such as fires or explosions [2]. Considering possible internal and external causes, it is crucial to better assess thermal runaway to reduce potential hazards in future advancements and safeguard the environment and people [3].

The behavior of Li-ion batteries under such thermal runaway reactions is influenced by their chemistry and state of charge (SOC). Key chemistries, such as lithium cobalt oxide (LCO), lithium nickel manganese cobalt oxide (NMC), and lithium iron phosphate (LFP), largely determine the behavior of the battery. LCO cathodes, known for their high energy density, are commonly found in portable electronics but are more reactive under stress. LFP cathodes, favored in electric vehicles

[☆] This manuscript has been authored in part by UT-Battelle, LLC, under contract DE-AC05-00OR22725 with the US Department of Energy (DOE). The US government retains and the publisher, by accepting the article for publication, acknowledges that the US government retains a nonexclusive, paid-up, irrevocable, worldwide license to publish or reproduce the published form of this manuscript, or allow others to do so, for US government purposes. DOE will provide public access to these results of federally sponsored research in accordance with the DOE Public Access Plan (<http://energy.gov/downloads/doe-public-access-plan>).

* Corresponding author.

E-mail address: wangh2@ornl.gov (H. Wang).

and grid storage, offer superior thermal stability and safety at the expense of lower energy density [2]. Meanwhile, the anode—typically made of graphite—provides a stable host for lithium-ion intercalation. The SOC also has a significant impact on safety. At higher SOCs, the battery holds more stored energy. This elevated energy state increases reactivity, making the battery more prone to severe thermal events during abuse. For instance, under mechanical stress, a high SOC leads to faster heat generation and larger voltage drops, escalating the risk of runaway reactions [2].

Numerous regulations have been implemented to provide a standard in battery safety, in particular through tests inflicting abuse on different battery scales (cell, module, entire pack) [4–6]. Such methods are typically conducted in a controlled environment, enabling comparable results for specific types of batteries. Notably, experimental results showed that the severity of thermal runaway was mainly influenced by the state of charge (SOC) [7]. Oak Ridge and Sandia National Laboratories have developed a single-side indentation protocol to mechanically abuse a battery cell, inducing an internal short circuit (ISC). Voltage and temperature curves are used to evaluate the battery's calculated hazard severity (CHS) and categorize them by observed hazard severity (OHS) like the EUCAR table [8,9]. The identification of a cell's severity contributes to the establishment of databases and enhances understanding of potential risks regarding thermal runaway in Li-ion batteries [10,11].

Databases offer partial assistance in grading battery behavior. However, building a comprehensive database takes tremendous, long-lasting efforts and costs since LIBs have many types, form factors, and capacities that are still being actively developed in academic laboratories and industry. Most thermal runaway studies [7,12–20] involve a limited number of cells of 1–2 chemistries. Usually, the data is not comparable due to the differences in test setup and data analysis. The ORNL/Sandia test protocol suggests a unified standard to integrate different experimental data for mechanically abused LIB cells. A well-controlled mechanical indentation testing method was leveraged and led to a simple but effective correlation analysis between cell SOC and its CHS [8,10]. The user-accessible thermal runaway database from mechanical indentation tests will continuously grow, and the users can rank and predict a LIB cell's thermal runaway severity in identical mechanical abuse conditions by utilizing the database contents or conducting a limited number of experiments since the extensive data points in the database will provide the fundamental intercalate support.

Beyond evaluating thermal runaway severity, the detection and prediction of thermal runaway are critical for implementing preventive measures. Non-destructive evaluation techniques, such as infrared (IR) imaging and passive acoustic emissions (AE) sensing, offer a promising approach for this purpose. Unlike traditional thermal couples that measure the temperature at a specific points, IR camera can detect the entire temperature field of an object with no physical contact needed, and was leveraged to monitor the battery surface temperature [21] or internal temperature change [22]. In this work, IR imaging was used to obtain the cell temperature next to the indenter and the surface temperature mapping evolution was analyzed. The AE has been used in the field of structural engineering to monitor different failure mechanisms such as matrix cracking, fiber break, fiber/matrix interface debonding, and interlaminar crack in polymer-matrix composites [23,24]. Prior research has demonstrated the potential of AE analysis in LIBs to monitor the formation of the solid-electrolyte interphase on the anode and cathode, electrode material degradation, and electrode delamination [25–30]. Schweidler et al. successfully correlated the acoustic events with various processes by monitoring and clustering the AE signals through the cycles of Li-ion battery [25,31]. More recently, AE analysis has been employed to investigate mechanical failures in batteries [30,32–34]. In this study, we extend the application of IR imaging and AE sensing to mechanical abuse testing induced by single-side cell indentation. To ensure continuous acoustic data acquisition while shielding the AE sensors from high temperatures and gas release, a magnetic steel plate was used as a waveguide between the sensors and

the test cell. 2D temperature maps from IR imaging and records of AE waveforms were synchronized with cell voltage measurements, delivering multifaceted diagnostic insights into the mechanically induced failure of Li-ion batteries. AE signals were detected prior, during, and after the onset of the ISC and the number of emissions qualitatively correlated with the severity of the thermal runaway. Overall, we show that IR imaging and AE sensing provide orthogonal data streams to conventional voltage measurements during mechanical abuse testing, which can contribute to an early detection of thermal runaway risk.

2. Test method

2.1. Li-ion batteries

Commercially available Li-ion cells were purchased from [Battery space.com](#), a Japan-based battery distributor. Three different chemistries were selected. The LCO and LFP cells capacities are new additions to the database [10,35], while the 10 Ah-capacity NMC cells have a different form factor to the previous NMC cells of the same capacity.

2.2. Acoustic emissions monitoring system

AE monitoring involves detecting transient, stress-induced acoustic signals or vibrations emitted by materials, which may reveal insights into phenomena within batteries that are difficult to observe with the naked eye [23]. Sensors are applied to detect these AE events by converting mechanical wave energy into electrical signals. Table 2 lists the two AE sensors utilized in this work for monitoring the acoustic signals during the battery mechanical indentation test.

The AE system includes the sensors, preamplifiers, a multi-channel data acquisition unit and the data processing software Vallen AE Suite (R2015) installed in a computer. Fig. 1 illustrates the AE system components and their cable connections.

An important parameter to measuring AE is setting a reasonable threshold (dBs), which filters unwanted data (e.g., mechanical movement, background noise) from experimental acoustic signals. In the current application, the threshold is set as 40 dB, as no AE hits were detected during a control experiment, in which the indenter contacted the LIB pouch cell surface with a small force (~5 pounds). Fig. 2 shows a typical hit signal captured by the AE sensor. The hit starts from when the AE first crosses the threshold line and ends at the last threshold crossing moment [36]. The time span between the hit start and end points is the duration. During the hit duration, the number of positive threshold crossings is defined as the counts, while the highest recorded voltage during the hit is defined as the peak amplitude. The signal rise time is the time difference between the peak occurrence and the start of the hit. Integrating the squared voltage of the recorded AE signal over the hit time duration yields the energy for this time slice.

2.3. IR monitoring device

Infrared thermography is based on the physical phenomenon that any body of a temperature above absolute zero (-273.15°C) emits electromagnetic radiation, and the radiation intensity is correlated to its temperature [37]. The non-contact nature of this technique makes it suitable to detect energy release in a Li-ion cell after the initiation of an internal short circuit. The early IR imaging technique relied on a single-point detector and a scanning mechanism. Even the fastest imaging device took significant time (10s of millisecond) to capture a surface temperature map. There is a time delay of the first pixel and the last pixel making it hard to be used for any object with rapid surface temperature changes. The first focal-plane-array (FPA) based thermographic devices for non-military application were available in the 1990s. The FPA detector allows all the pixels to be exposed to the thermal radiation at the same time and for the same amount of time, enabling high-speed and high-resolution IR imaging. After decades development, the infrared

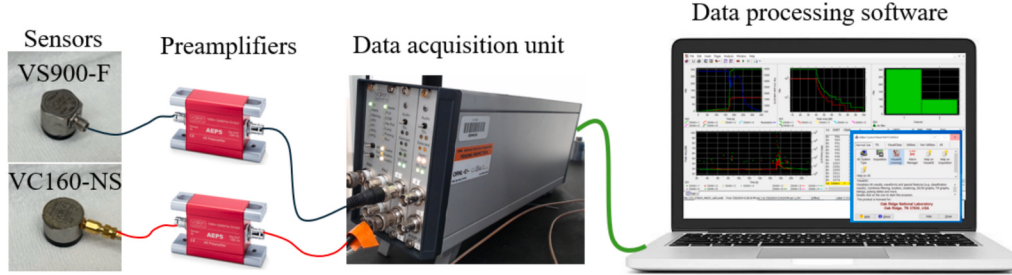


Fig. 1. AE system illustration.

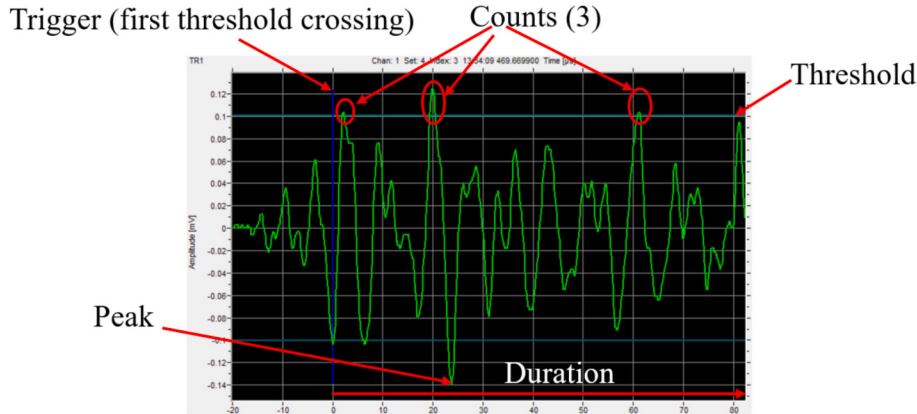


Fig. 2. Illustration of an AE hit signal with labeled threshold, peak amplitude, duration, counts features.

cameras on the market now become compact with greater mobility, sensitivity, measurement accuracy and more software functionalities. In this work, the FLIR A325 was used along with its ResearchIR software to capture the real-time full field temperature change through the battery indentation test. It used an uncooled microbolometer FPA capable of recording 16-bit 320×240 pixels thermal images at rates up to 60 Hz. Using two internal neutral density filters, three temperature ranges could be selected from -20 to 1200 °C.

2.4. Test protocol

The cells individually underwent cycling between 3 and 5 times at C/2 from 3.0 to 4.2 V through channels of a Bitrode MCV™ cycler and then discharged to the desired SOCs. The Servo-motor test system under the displacement control mode with a speed of 0.05 inches per minute was then applied to each cell for mechanical indentation test. The LabView™ software regulated a load frame applying single-side indentation on the battery, capturing load and voltage data. An infrared camera (FLIR A325) monitored the surface temperature of the cells [8]. Though the infrared camera could run up to 60 Hz, the stored images were captured at 4 Hz in these tests to reach a balance between limited storage and necessary resolution in time scale. To achieve a better temperature resolution of 0.2 °C in the temperature range between the ambient temperature (~ 20 °C) and the separator melting temperature (~ 150 °C), the maximum temperature limit of the infrared camera was set to 360 °C. The surface emissivity of the battery was set to 0.9 based on the calibration using a thermocouple with a fixed camera distance and view factor. These programs were manually controlled and self-regulated. A 6" × 6" magnetic steel plate was placed between the test battery and the load cell to not only protect the load cell from the battery thermal runaway, but also act as a waveguide to transfer the AE signals to the AE sensors attached to the plate. The Vallen System AE setup primarily consisted of two sensors — the VS900-F and VC160-NS listed in Table 2, two AEP5 preamplifiers, one data acquisition unit,

connecting wires, and a laptop equipped with the Vallen software suite. In addition to the AE setup, the cell voltage signal was collected by the Vallen System to synchronize the AE measurement with the time series recorded in the LabView™ software. The vacuum grease was applied to the bottom surface of the test LIB cell to improve the contact between the battery and steel plate and thus the transferability of acoustic signals. Precautions such as aluminum foil around the AE sensors and cables were taken to protect the equipment from overheating and gas release during the thermal runaway. Fig. 3 showed the test setup. Particularly, the magnetic holder tightly attached the AE sensor on the steel plate surface. The acoustic sensors are encapsulated in an aluminum foil as displayed in Fig. 3.

The single-side cell indentation test followed the test protocol listed in Table 3. More technical details of these protocols can be found in literature [8,10]. Note that the blunt indenter, slow loading speed, and the short-circuit detection small voltage drop threshold slowed down the self-discharge through the ISC creating a more controllable thermal runaway in the laboratory environment. As an additional monitoring device, the AE data acquisition unit synchronized the data acquisition with the load frame and infrared camera from the same beginning time.

3. Thermal runaway severity grading

The compression from the slow-moving indenter created internal layer damage within the pouch cell, resulting in a short-circuit inside and a drop in cell voltage. In some cases, the heat generated by the ISC may trigger additional physico-chemical reactions, swelling the cell itself and causing more internal damage. The indenter could even penetrate through the cell layers and a significant amount of smoke, flame and gas might burst out if severe thermal runaway occurred. All these complex effects, along with cell's chemistry, form factor, capacity, SOC etc. turned the grading of thermal runaway severity into a challenge. The European Council for Automotive R&D (EUCAR), a consortium of European automotive manufacturers, has investigated the hazards that

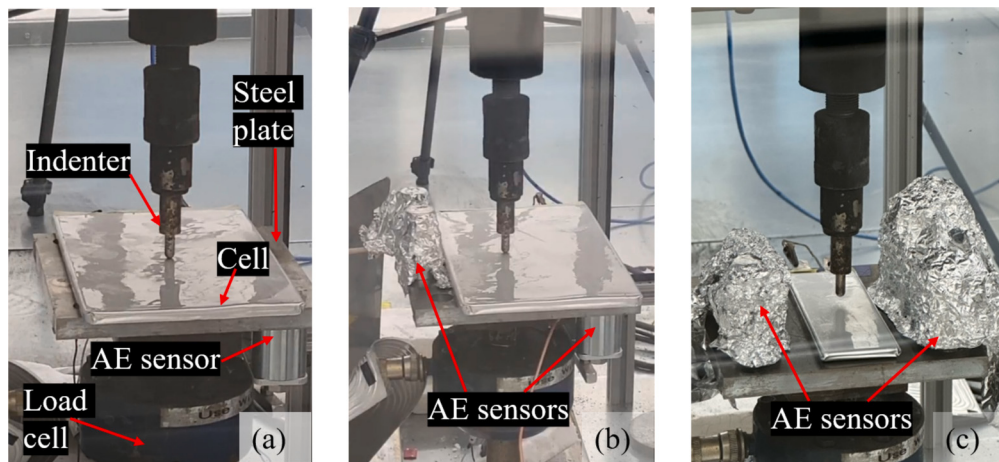


Fig. 3. Test setup and AE sensors, (a) LFP cell with one AE sensor attached under the plate, (b) LFP cell with two AE sensors, (c) LCO cell with two AE sensors.

Table 1
Tested cells.

Cell type	Cathode	Anode	Cell dimensions (thickness × width × length, mm)	Capacity (mAh)	Quantity
LCO	LiCoO ₂	Graphite	5 × 43 × 130	4000	18
LFP	LiFePO ₄	Graphite	5 × 121 × 190	15,000	13
NMC	LiNiMnCoO ₂	Graphite	6 × 91 × 141	10,000	13

could arise when testing batteries and divided them into eight classes in [Table 4](#) [9]. Some criteria, such as the weight loss, were easy to measure and quantify. However, most of the classification criteria were based on visual and physical examination which heavily relied on the technician's experience.

To address this difficulty, the ORNL-Sandia approach modifies the EUCAR hazard level system to better utilize data from thermal runaway incidents. Cell temperature and open circuit voltage were the two major measurements that recorded the battery dynamics through the mechanical abuse test. A new quantitative grading system, combining the initial cell voltage, the final voltage, the critical voltage drop during the ISC, the maximum temperature through the test, the maximum temperature increase rate, the battery capacity and the SOC into a calculation that returned a score number in range of 5 to 100. Given a specific thermal runaway severity score, the grade of cell hazard severity level can further be categorized into five grades which are very low (VL, 0–10), low (L, 10–25), moderate (M, 25–75), high (H, 75–90) and very high (VH, 90–100) respectively [8]. Our previous work [8,10] has demonstrated that this grading system can effectively characterize cell's overall thermal runaway risk under mechanical abuse tests, improving the vague criteria in EUCAR by precise and rigorous experimental measurements. By following the same test protocols and thermal runaway severity calculation, the cells listed in [Table 1](#) with different SOCs were tested and their resulting CHS scores and hazard levels are summarized in [Table 5](#).

The CHS scores for these cells are summarized in [Fig. 4](#). Although the LFP cells have the largest capacity among three cell chemistries in [Table 1](#), they yielded lower CHS than the other two cell chemistries for the same SOC and only moderate CHS even at the fully charged state (100 % SOC). Both NMC and LCO cells demonstrated severe thermal runaway at high SOCs despite having a smaller capacity than the LFP cells. The 'Very High' hazard level was recorded from the LCO cells with SOC higher than 50 %, while this critical threshold shifted to 70 % SOC for the 10 Ah NMC cells.

Table 2
Applied AE sensors.

Type	Frequency range (kHz)	Shape	Max. operating temp (°C)
VS900-F	100–900 (high)	Pentagonal	150
VC160-NS	100–450 (low)	Circular	180

Table 3
ORNL-Sandia test protocols [8].

Test subject	<ul style="list-style-type: none"> Single Li-ion pouch cells Capacity range: 0.5 Ah–33 Ah Stainless steel sphere or blunt indenter presses on pouch center Diameter: 6 mm for standard test and 12.7 mm for occasional comparison test Cell support: Stainless steel block Motor-driven or hydraulic loading system Speed: 0.05 in/min (1.27 mm/min) Open circuit voltage: V_{oc} Load Displacement Cell surface temperature (next to the indenter) and multiple points on the surface, temperatures of positive/negative tabs measured by thermocouples or IR imaging
Indentation	
Loading	
Measurements/monitoring, DAQ rate at 10 Hz or faster	
Short-circuit detection and post-triggering actions	<ul style="list-style-type: none"> Voltage drop $V_{oc} \geq 25$ mV Indenter stay in place for >10 min Keep recording V_{oc}, temperature, load and displacement for >5 min

4. Temperature mapping and acoustic emissions detection during thermal runaway testing

The mechanical indentation causes structural deformation and local penetration, triggering the ISC that leads to thermo-chemical interactions within the LIB cell. When the accumulated heat generation from exothermic reactions exceeds heat dissipation, the thermal runaway emerges with a substantial temperature rise and violent gas release. ISC-driven physical activities often yield an energetic signature, which can manifest as both thermal and acoustic signals. When the energy waves are transmitted to the cell surface and the environment, the thermal and acoustic signals can be detected by an infrared camera as surface temperature maps and an acoustic sensor as AEs.

[Fig. 5](#) shows infrared camera images taken immediately after the initial voltage drop on a 4 Ah-capacity LCO cell at 90 % State of Charge (SOC). A very non-uniform temperature pattern developed within 1.25 s followed by a violent thermal runaway (CHS = 100).

For the 10 Ah-capacity NMC cells, the 30 % SOC cell demonstrated a

Table 4
EUCAR hazard severity levels [9].

Hazard level	Description	Classification criteria & effect
0	No effect	No effect. No loss of functionality.
1	Passive protection activated	No defect; no leakage; no venting, fire, or flame; no rupture; no explosion; no exothermic reaction or thermal runaway. Cell reversibly damaged. Repair of protection device needed.
2	Defect/damage	No leakage; no venting, fire or flame; no rupture; no explosion; no exothermic reaction or thermal runaway. Cell irreversibly damaged. Repair needed.
3	Leakage $\Delta m_{\text{ass}} < 50\%$	No venting, fire, or flame; no rupture; no explosion. Weight loss < 50 % of electrolyte weight (electrolyte = solvent + salt).
4	Venting $\Delta m_{\text{ass}} \geq 50\%$	No fire or flame; no rupture; no explosion. Weight loss $\geq 50\%$ of electrolyte weight (electrolyte = solvent + salt).
5	Fire or flame	No rupture; no explosion (i.e., no flying parts).
6	Rupture	No explosion, but flying parts of the active mass
7	Explosion	Explosion (i.e., disintegration of the cell).

gradual temperature increase over 10 s. (Fig. 6a, b). The insets of Fig. 6a and b show the temperature profiles along the line through the indentation point at 0 and 10 s. Both temperature profiles are symmetric, indicating radial heat conduction from the localized Joule heating at the indentation point to the surrounding pouch cell. The CHR score of this tested cell was 42. In contrast, the NMC 10 Ah cell charged to 100 % State of Charge (SOC) initially demonstrated a non-uniform temperature distribution with double peaks (Fig. 6c). Within 1 s, the temperature increased rapidly, and the temperature profile changed to almost one single peak across the width direction (Fig. 6d). Then, the cell went to full-scale thermal runaway, resulting in a CHR score of 100. Finally, Fig. 6e–g shows three IR camera images from mechanical indentation testing of a 15 Ah-capacity LFP cell of 10 % SOC taken at 1, 5, and 10 s. Similar to the IR camera images of the NMC 30 % SOC cell in Fig. 6a and b, the concentric circles emerge and expand from 1 to 10 s, representing the gradual radial heat conduction. The CHR score of the cell was 34. Note that the LFP cells at higher SOCs, even for fully charged cells of 100 % SOC, demonstrated similar thermal signatures with gradual temperature rise.

AE sensing provides an additional degree of thermal runaway monitoring, complementing voltage and temperature measurements. Figs. 7 and 8 illustrate the AEs synchronized with the cell voltage and temperature profiles of three different pouch cells for 0 % SOC and 100

Table 5
Test results of three different cells in various SOCs.

Chemistry	SOC (%)	Cells	Capacity (Ah)	Calculated hazard severity (CHS)	Hazard level
LCO	0	Cell 1	4	31.80	Moderate
		Cell 2	4	26.77	Moderate
	10	Cell 1	4	55.16	Moderate
		Cell 2	4	42.30	Moderate
	20	Cell 1	4	50.22	Moderate
		Cell 2	4	44.86	Moderate
	30	Cell 1	4	45.06	Moderate
		Cell 2	4	58.20	Moderate
	40	Cell 1	4	62.50	Moderate
		Cell 2	4	53.35	Moderate
	50	Cell 1	4	100.00	Very high
		Cell 2	4	100.00	Very high
NMC	60	Cell 1	4	61.24	Moderate
		Cell 2	4	100.00	Very high
	70	Cell 1	4	100.00	Very high
		Cell 2	4	100.00	Very high
	80	Cell 1	4	100.00	Very high
		Cell 2	4	100.00	Very high
	90	Cell 1	4	100.00	Very high
		Cell 2	4	100.00	Very high
	100	Cell 1	4	100.00	Very high
		Cell 2	4	100.00	Very high
LFP	0	Cell 1	10	37.91	Moderate
		Cell 1	10	39.81	Moderate
	10	Cell 1	10	5.00	Very low
		Cell 1	10	41.78	Moderate
	20	Cell 1	10	41.61	Moderate
		Cell 1	10	49.17	Moderate
	30	Cell 1	10	46.44	Moderate
		Cell 1	10	54.99	Moderate
	40	Cell 1	10	100.00	Very high
		Cell 2	10	37.97	Moderate
	50	Cell 1	10	62.17	Moderate
		Cell 1	10	100.00	Very high
	60	Cell 1	10	100.00	Very high
		Cell 2	10	100.00	Very high
	70	Cell 1	10	100.00	Very high
		Cell 2	10	100.00	Very high
	80	Cell 1	10	100.00	Very high
		Cell 2	10	100.00	Very high
	90	Cell 1	10	100.00	Very high
		Cell 1	10	100.00	Very high
	100	Cell 1	10	100.00	Very high
		Cell 2	10	100.00	Very high
	0	Cell 1	15	14.27	Low
		Cell 1	15	35.90	Moderate
	10	Cell 1	15	34.03	Moderate
		Cell 1	15	41.11	Moderate
	20	Cell 1	15	32.60	Moderate
		Cell 2	15	43.82	Moderate
	40	Cell 1	15	41.10	Moderate
		Cell 2	15	46.25	Moderate
	50	Cell 1	15	49.62	Moderate
		Cell 2	15	55.45	Moderate
	60	Cell 1	15	53.31	Moderate
		Cell 2	15	68.77	Moderate
	80	Cell 1	15	65.29	Moderate
	100	Cell 2	15		

% SOC, respectively. The plotted temperature is the maximum temperature extracted from each 2D temperature frame continuously recorded by the IR camera. First, for the 0 % SOC cases, a limited number of AE hits (solid or empty circles in the figures) were detected in all tested cathode chemistries (LCO, LFP and NMC cells). Compared to LCO and LFP cells, the NMC 10 Ah cell demonstrated more AE hits before the onset of the ISC. This observation implies that more severe internal interactions occurred in the NMC cell before the onset of the ISC. A small temperature increase before 300 s of NMC 0 % SOC cell in Fig. 7c corroborates this proposition. The total number of hits for these three cells was 12 from Sensor 1, 30 from Sensor 2 for LCO, 108 from Sensor 1, 90 from Sensor 2 for LFP, and 146 from Sensor 1, 86 from Sensor 2 for NMC, respectively (see Table 6). A significant burst of AE hits was observed when the steep voltage drop and temperature rise occurred, representing an instantaneous energy release at the onset of the ISC. Fewer AE hits were recorded afterward. All the 0 % SOC cases demonstrated low or moderate levels of thermal runaway risk, as calculated by their CHS, despite the dynamic response of voltage drop and temperature rise varied with cathode chemistries.

Unlike the 0 % SOC cases, more AE hits were detected from the 100 % SOC cases. The total number of measured AE hits (Table 6) was 520 from Sensor 1 and 360 from Sensor 2 for the LCO cell, 271 from Sensor 1 and 118 from Sensor 2 for the LFP cell, 671 from Sensor 1, and 654 from Sensor 2 for the NMC cell, respectively. The LCO 100 % SOC cell demonstrated a considerable number of AE hits before the onset of ISC at about 176 s. AEs from the LCO 100 % SOC cell also contain high-magnitude signals up to 100 dB, which can be attributed to a violent

release of gas and smoke due to strong thermal runaway activated in the LCO 100 % SOC cell. Note that temperature plateau of 360 °C around 200 s in Fig. 8a was due to the upper limit of the infrared camera temperature measurement. Hence, the temperature during this 360 °C plateau should be above 360 °C. Nevertheless, CHS was not affected by the temperature limit because the temperature already exceeded the threshold that determines the occurrence of the thermal runaway. Next, the LFP 100 % SOC cell exhibited a few AE hits prior to the onset of ISC near 170 s. Larger number and greater amplitude of AEs are concentrated at the onset of ISC than before or after this point for the LFP 100 % SOC cell. The highest amplitude of the AEs was 73 dB and the hit duration was approximately 10 s (from 165 s to 175 s). Specifically, the voltage of this LFP cell dropped from 3.35 V to 3.26 V and then bounced back to 3.29 V whereas voltage of the LCO and NMC cells immediately plummeted to 0 V after the onset of ISC. While severe thermal runaway with significant gas and smoke release occurred from the LCO and NMC 100 % SOC cells, only local swelling around the indentation hole was observed from the LFP 100 % SOC cell. Simultaneously, the temperature rise from the LFP cell remained below 90 °C even after its voltage drop (~0.09 V), which is significantly lower than those of the LCO and NMC 100 % SOC cells. Third, the NMC 100 % SOC cell demonstrated less AE hits before the onset of ISC compared to its 0 % SOC counterpart. Numerous AE hits are recorded at and after the onset of ISC, including a significant number of high-magnitude AEs above 50 dB recorded during thermal runaway as shown in Fig. 6c.

5. Discussion

The single side indentation test provided consistent results for investigating thermal runaway risk for large-format pouch cells with varying SOC. Utilizing the voltage and temperature measurements through the test, the CHS quantified the thermal runaway severity which agreed with visual observations (degree of pouch swelling, cell color change due to heat, smoke and gas generation) in the tests. The five severity levels categorized by the CHS scores enhanced the ambiguous definition of thermal runaway hazard in EUCAR, enabling the quantitative comparison of the thermal runaway severity of large-format pouch cells across different electrode chemistries, capacities and SOCs. In addition, the correlation between CHS and SOC can be used to predict

Table 6
Number of AE hits in indentation test.

		Sensor 1	Sensor 2
0 % SOC	LCO 4 Ah cell	12	30
	LFP 10 Ah cell	108	90
	NMC 10 Ah cell	146	86
100 % SOC	LCO 4 Ah cell	520	360
	LFP 10 Ah cell	271	118
	NMC 10 Ah cell	671	654

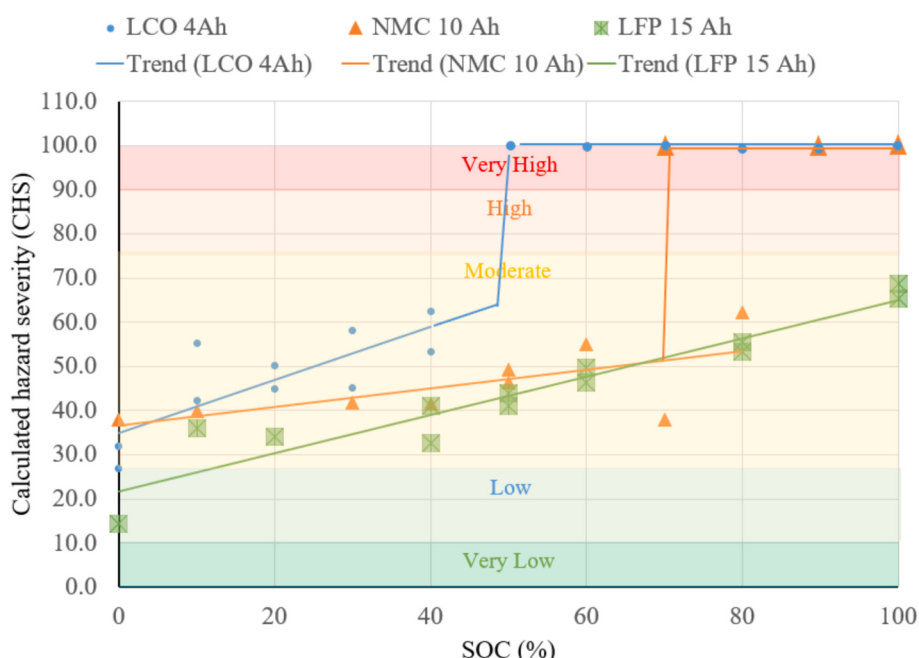


Fig. 4. Calculated hazard severity of three different types of cells and their trend lines (solid lines).

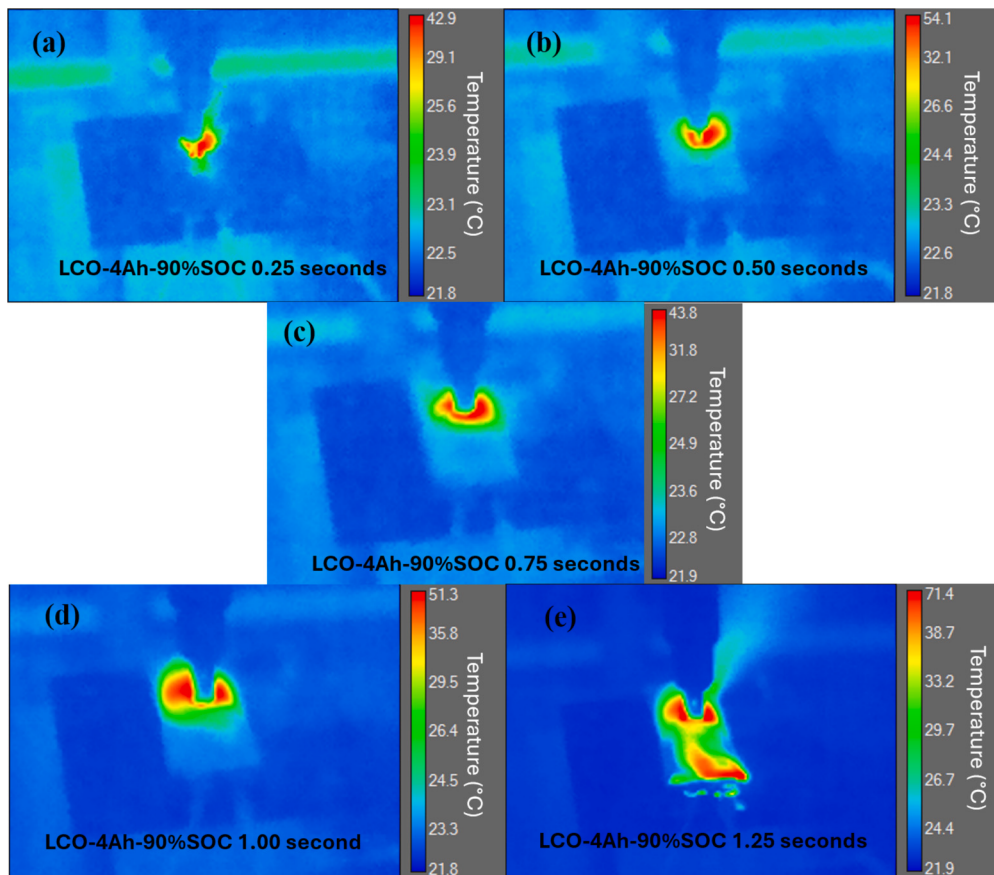


Fig. 5. Infrared images captured rapid, non-uniform temperature changes with 1.25 s of short circuit in LCO 4 Ah 90 % SOC cell, (a) 0.25 s, (b) 0.50 s, (c) 0.75 s, (d) 1.00 s, and (e) 1.25 s.

the thermal runaway risk of the LIB with specific electrode chemistries and SOCs. The linear regression curves shown in Fig. 4 represent this correlation where the hazard level is lower than “Very High” severity, i.e. the thermal runaway. The formulas for these linear regression curves are shown in Eqs. (1)–(3) for the LCO 4 Ah cells, the NMC 10 Ah cells, and the LFP 15 Ah cells. The slopes or the linear coefficient of CHS to SOC represent the severity growth rate with SOC. The LCO 4 Ah cell demonstrated a greater slope than the two other higher capacity cells (NMC 10 Ah and LFP 15 Ah) for a non-thermal runaway regime where CHS is below 100. This linear trend indicates that with higher SOC, more electrical energy is released as heat due to the internal short circuit, which is reflected in the overall temperature increase, the temperature increase rate, the voltage drop, and the voltage drop rate. Our previous work [8,10] shows more details of using all these test measurements to calculate the thermal runaway score. The empirical equations to include cell capacity, SOC, temperature and voltage variables may result in the linear relationship between the score and the SOC. However, this trend may vary across cell types and capacities. As illustrated in Fig. 4, the LCO 4 Ah and NMC 10 Ah cells exhibit different slope magnitudes (0.60 and 0.21, respectively). We acknowledge that the regression fitting accuracies for these two types of cells are relatively low ($R^2 = 0.63$ for LCO 4 Ah and $R^2 = 0.45$ for NMC 10 Ah), which is due to the limited data points (~10) at Low and Moderate severity levels. Additionally, these cells have a higher energy density and lower thermal stability compared to LFP cells, contributing to greater variability in their response to indentation testing. These limitations underscore the inherent difficulty in repeating identical indentation tests with minimal data deviation. The SOC thresholds over which CHS equals 100, i.e. thermal runaway, are 50 % and 70 % for the LCO 4 Ah and the NMC 10 Ah cells, respectively. Both LFP and NMC cells had smaller correlation slopes (0.43 and 0.21,

respectively) than the LCO cells (0.60), however the LFP cells did not go to full thermal runaway even when they were fully charged (100 % SOC). Note that the data points with CHS = 100 were excluded in linear regression analysis. The data point (20 % SOC, 5 CHS) was not included in the NMC regression due to its abnormal voltage recovery and low temperature through the test.

$$CHS_{LCO} = \begin{cases} 0.60 \times SOC + 34.99, & SOC < 50 \\ 100, & SOC \geq 50 \end{cases} \quad (1)$$

$$CHS_{LFP} = 0.43 \times SOC + 21.76 \quad (2)$$

$$CHS_{NMC} = \begin{cases} 0.21 \times SOC + 36.63, & SOC < 70 \\ 100, & SOC \geq 70 \end{cases} \quad (3)$$

To validate the linear regression, a new LCO 4 Ah cell at 20 % SOC was tested which returned a CHS of 34.26 using the CHS formula defined in our previous work. [8,10] Eq. (1) predicts this CHS to be 49.28, which yields a prediction error of 43.8 %. Compared to the two LCO 4 Ah cells of 20 % SOC in Table 5, this validation LCO cell demonstrated a mild reaction in voltage and temperature response due to mechanical indentation. A new LFP 15 Ah cell at 30 % SOC was tested for the same validation purpose. The predicted CHS for this LFP cell was 34.66 using Eq. (2), while the CHS formula of our previous works yielded 34.95. The error between the predicted and actual CHS was –0.8 %. The dispersion of the data for LCO/NMC cells was increased due to the fact that their inherent response to the indentation is more sensitive than LFP cells. Eqs. (1)–(3) reflect the trends between cells’ SOC and their CHS at current testing conditions. These predicting equations should be used with care due to the dispersion and limited number of data points. More cell indentation data are needed and that is a challenging and

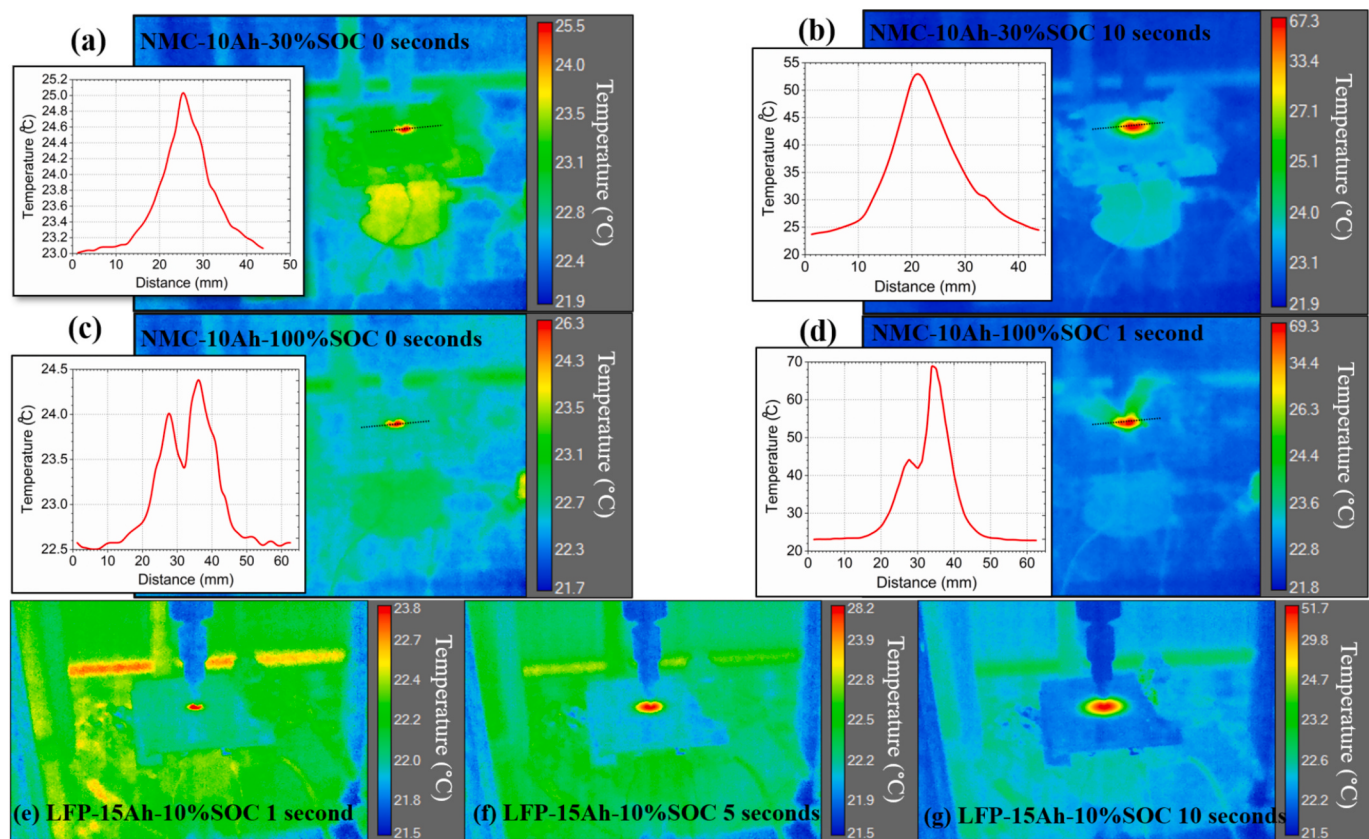


Fig. 6. Infrared imaged and line profiles of NMC 10 Ah and LFP 15 Ah cells after short circuit, (a) NMC 30 % SOC cell at 0 s, (b) NMC 30 % SOC cell at 10 s, (c) NMC 100 % SOC cell at 0 s, (d) NMC 100 % SOC cell at 1 s, (e) LFP 10 % SOC cell at 1 s, (f) LFP 10 % SOC cell at 5 s, and (g) LFP 10 % SOC cell at 10 s.

continuous effort towards providing quantitative CHS predictions. Additional tests of LCO and NMC cells with higher SOCs, such as 60 % SOC for LCO, 80 % SOC for NMC, returned CHS = 100 with strong thermal runaway response, which validates the CHS grading system and the thermal runaway severity analysis presented in this work.

To monitor the energy release from the pouch cells abused by mechanical indentation, we introduced two distinct methods to capture two unique responses: 1) dynamic temperature distributions and 2) acoustic emissions. First, the 2D temperature maps by IR camera delineated the thermal energy generation and dissipation from the pouch cells. By analyzing the temperature maps frame-by-frame, heat transfer patterns and thermal signatures associated with thermal runaway risk are revealed. Gradual heat conduction parallel to the battery layers was observed from LFP cells and low-SOC NMC cells, implying that Joule heating from the ISC did not trigger the cascading exothermic reactions leading to thermal runaway. The temperature rise was moderate, and the cells were slowly discharged to zero voltage via the ISC. The discharge process could take hours depending on the contact resistance and the cells would not enter thermal runaway. For the NMC and LCO cells at higher SOC, the temperature distribution immediately after the onset of ISC was heterogeneous and the heat transfer was rapid, indicating exothermic reactions within the cell. Since exothermic reactions generated significant gas which inflated the pouch cell, the surface temperature measured by the IR camera did not represent the exact temperature of the inner battery layers due to high thermal resistance of additional gas layer. Nevertheless, the 2D temperature maps from the high-SOC case contain unique features that are distinct from the gradual heat conduction in the low-SOC cases.

Second, the AE sensing enables a new method to monitor acoustic energy emanated from the internal degradation and fracture of pouch cells provoked by mechanical indentation. Several AE hits were

collected before the onset of ISC, whereas the number of hits increased at and after the onset of ISC. The AE hits plotted with voltage and maximum temperature profiles shown in Figs. 7 and 8 were highly concentrated at the onset of ISC indicated by the abrupt voltage drop and temperature spike. Regardless of the initial SOC, the AE signals with the largest amplitude, maximum counts, and longest duration were detected at this critical point. Combined with the CHS grading system, the AE measurement could improve the evaluation of thermal runaway risk.

The AEs before the critical onset of the ISC also reveal characteristic differences among the three cathodes tested in this work. The LCO cell generated fewer AE signals before the onset of the ISC at 0 % SOC. In contrast, a remarkable amount of AE signals was recorded in this period without voltage drop or temperature rise at 100 % SOC. In contrast, the NMC cell had more AE hits (19 for Sensor 1 and 13 for Sensor 2) before the onset of ISC at 0 % SOC than 100 % SOC (7 for Sensor 1 and 7 for Sensor 2), but after the onset of ISC, the 100 % SOC cell exhibited much more AE hits (86 for Sensor 1 and 94 for Sensor 2) than the 0 % SOC cell (5 for Sensor 1 and 4 for Sensor 2). The LCO cells demonstrated the largest AE amplitudes despite the lowest charge capacity, which aligns well with the calculated CHS of LCO cells. On the contrary, the LFP cells had the largest capacity, but the failure response was the mildest in terms of both CHS values and the AE amplitudes. For the case of 100 % SOC data in Fig. 8, the first AE hits were detected more than 100 s before the onset of an ISC where the cell surface temperature and voltage remained stable. The number of AE hits recorded during the mechanical indentation testing, particularly detected before and at the onset of ISC, appears to be correlated with the severity of the subsequent thermal runaway. These early AE signals have the potential to detect internal damage and enable intervention prior to thermal runaway. Correlating the waveform characteristics of AE signals with underlying internal

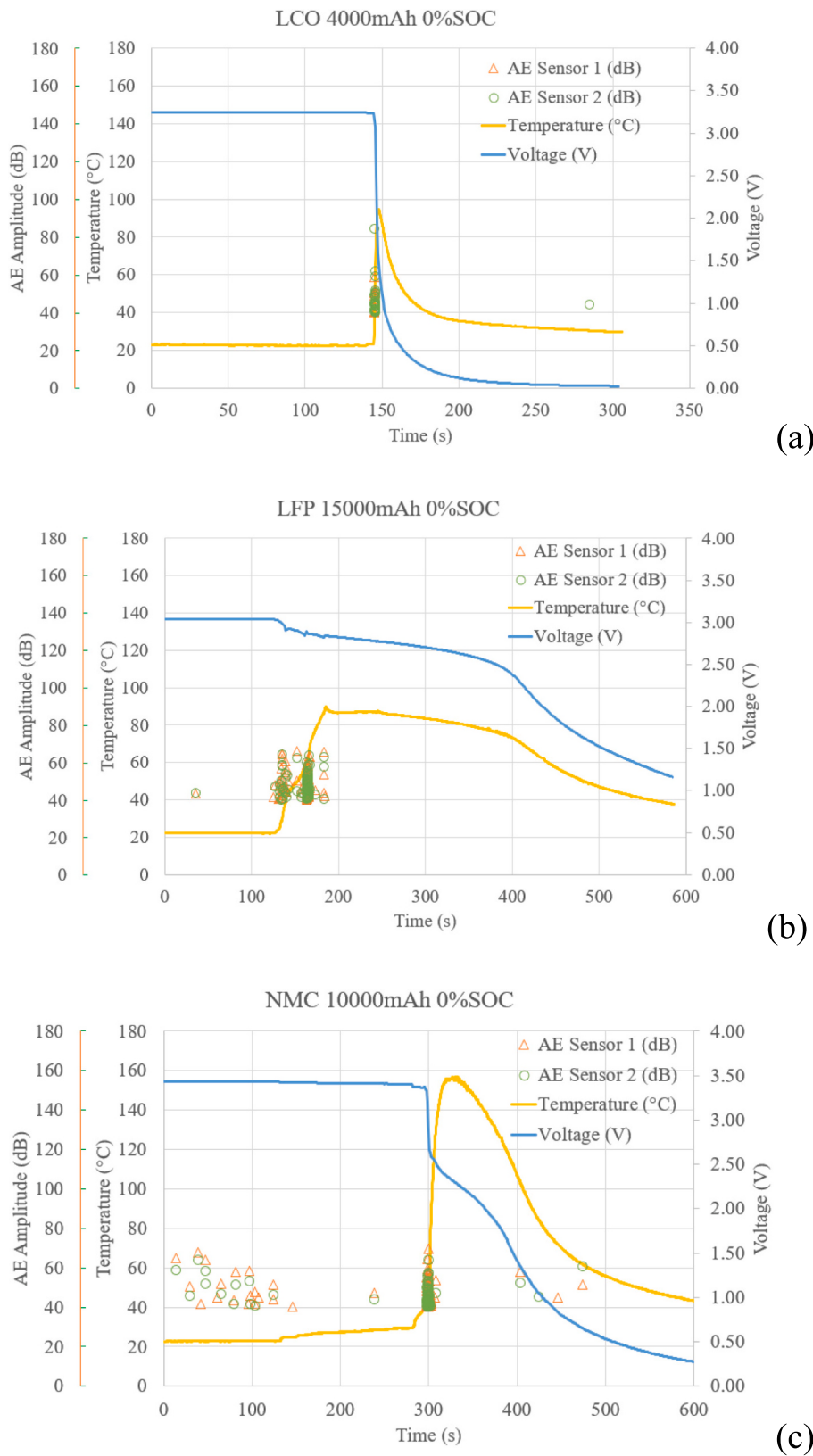


Fig. 7. AE signal amplitude and cell voltage, temperature, (a) LCO 4 Ah cell at 0 % SOC, (b) LFP 15 Ah cell at 0 % SOC, (c) NMC 10 Ah cell at 0 % SOC.

battery mechanisms may advance the development of accurate physics-based models for batteries undergoing thermal runaway and support the creation of practical battery safety metrics for real-world applications. A comprehensive analysis of these waveforms and their associated

mechanisms will be presented in a companion paper.

Several failure responses to mechanical indentation resulted in significant gas generation and pouch cell swelling, causing a pouch burst with high-temperature gas and smoke when the internal pressure

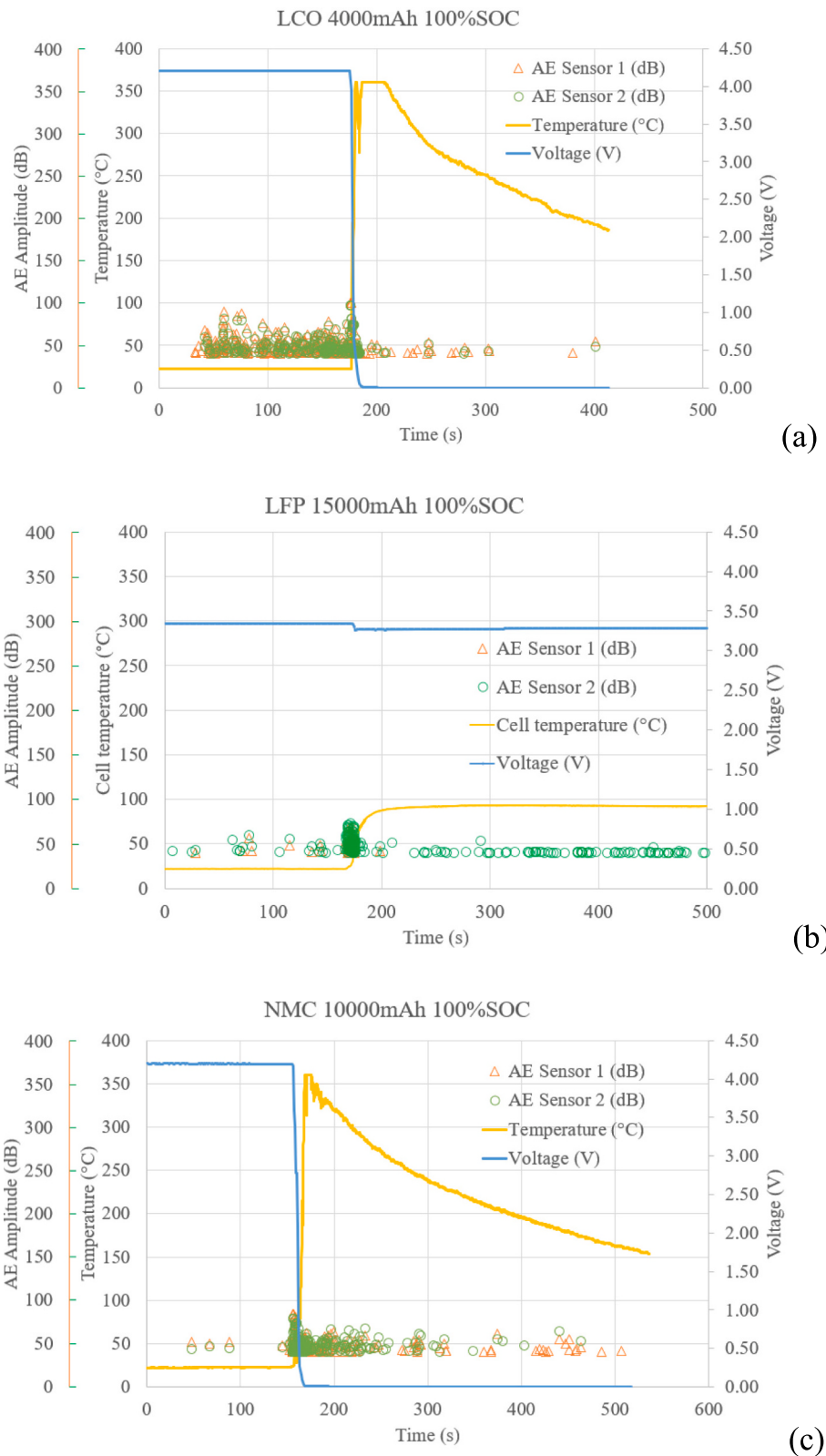


Fig. 8. AE signal amplitude and cell voltage, temperature, (a) LCO 4 Ah at 100 % SOC, thermal runaway, (b) LFP 15 Ah at 100 % SOC, local swelling (c) NMC 10 Ah at 100 % SOC thermal runaway.

exceeded the breaching threshold of the pouch sealing. Selected LCO cells after the mechanical indentation tests in Fig. 9 showed a residual inflation due to this process. In Fig. 9, the LCO cells also demonstrated a qualitative trend of higher temperatures and stronger inflation with

increasing SOC based on the degree of color change and swelling visible on the surface. As opposed to the LCO cells, there is negligible swelling and color change from LFP cells near the indentation hole. The significant color change and swelling occurred only on NMC cells with high



Fig. 9. Cells after indentation test, (a) LCO 4 Ah cells, (b) LFP 15 Ah cells, (c) NMC 10 Ah cells.

SOC, such as 90 % or 100 %. Note that the NMC cell pictures in Fig. 9 were taken with label side on top, illustrating no penetration holes at all those cells by following the test protocols.

Thermal runaway in Li-ion batteries occurs when the heat generation rate from Joule heating and exothermic reactions exceeds the heat dissipation rate, leading to a rapid, uncontrolled temperature increase [38,39]. Once the temperature reaches the onset threshold for exothermic reactions, a positive feedback loop is initiated, resulting in a significant amount of smoke, gas, flames, and potentially fire or explosion, depending on the battery's properties, capacity, SOC, and abuse environment. The chain reaction occurs across different exothermic reaction mechanisms, from the decomposition and regeneration of the solid electrolyte interphase (SEI) layer at intermediate temperatures (below 150 °C) to the decomposition of electrolyte and the cathode/anode reactions at elevated temperatures (above 150 °C) [40,41]. The internal short circuit is the primary driver that raises the battery temperature from ambient to the onset of the first exothermic reaction through Joule heating. Once the temperature reaches the separator melting point, additional internal short circuits occur throughout the cell, intensifying Joule heating and accelerating thermal runaway. The initial internal short circuit is typically caused by three types of abuse scenarios: mechanical, electrical, and thermal abuse [42]. The single-sided indentation test introduced in this work falls in the mechanical abuse category. The low-speed mechanical indentation gradually punctures the separators beneath the indenter, from the top layers down to the bottom, inducing the internal short circuit in a controlled manner. The synchronized voltage, temperature, and AE measurements implemented in this work capture the onset of internal short circuits, localized Joule heating near the indentation site, and extensive gas release in cells exhibiting high thermal runaway severity. These observations are further validated by the full-field temperature distributions and real-time videos. The single-sided indentation test, integrated with temperature mapping and AE, enables precise, diagnostic safety testing of internal short circuit and thermal runaway. More importantly, our approach generates high-quality data that can quantitatively categorize the thermal runaway severity of Li-ion battery pouch cells across varying capacities and SOCs.

6. Conclusions

The standard single-side indentation test was conducted with two non-destructive methods to monitor the energy release from the LIB pouch cells via the surface temperature distribution and the acoustic emissions. The CHS was also calculated to quantify the thermal runaway severity for different cathode chemistries and SOCs. As a result, higher SOC and more reactive cathodes, e.g. LCO, significantly intensified the failure response and triggered thermal runaway, demonstrated by rapid temperature increases, abrupt voltage drops, and amplified AE signals. The highest CHS was calculated from LCO cells that yielded rapid temperature escalation and significant gas release at higher SOCs. The CHS scores successfully correlated SOC of three cathode chemistries tested in this work to the thermal runaway severity of different levels, which can replace the ambiguous descriptions of the EUCAR table with quantified OHS in five categories (Very Low, Low, Moderate, High, Very High). Despite having the smallest capacity, the LCO 4 Ah cells had the highest chance to enter severe thermal runaway under the same indentation test conditions. The combination of high energy density and lower thermal stability renders the LCO cells highly reactive with rapid temperature escalation and significant gas release, especially at higher SOCs. In contrast, the LFP 15 Ah cells demonstrated the lowest risk into thermal runaway. Even at higher SOCs, LFP cells maintained thermal stability with slower temperature rise and no visible gas release, which is consistent with their low CHS scores for all SOCs. In current test configurations, the SOC shows a positive correlation to the CHS score. The trends could be used to predict CHS score for different cells with different SOCs, but more test data are needed to promise a consistent prediction. In addition to the CHS gradings, temperature maps showed two distinct heat transfer patterns that were associated with a gradual thermal conduction and an intense heat generation from exothermic side reactions. The newly introduced AE sensing successfully detected acoustic energy release throughout the indentation testing. The AEs can serve as precursors of thermal runaway, detecting internal degradation and fracture of LIBs unseen from the surface measurement. Meanwhile, surface temperature distributions recorded by IR camera can inform heat transfer patterns in LIBs as response to the ISC induced by mechanical indentation. Therefore, the continuous monitoring of energy release in two distinct physical signatures, temperature distributions

and acoustic emissions, provides critical insights into the relationship between internal degradation and external failure response of mechanically abused LIBs. Future work will involve the identification and classification of the AE signals in accordance with voltage profiles and temperature distributions.

CRediT authorship contribution statement

L. Lin: Writing – original draft, Methodology, Investigation, Formal analysis, Data curation, Conceptualization. **K. Hartono:** Data curation. **Y. Ko:** Writing – review & editing, Validation, Investigation, Data curation. **R. Mallela:** Data curation. **Y. Samantaray:** Writing – review & editing, Methodology. **H. Bouteiller:** Writing – review & editing. **M.Z. Bazant:** Writing – review & editing, Supervision, Methodology, Investigation. **H. Wang:** Writing – review & editing, Supervision, Resources, Project administration, Methodology, Investigation, Funding acquisition, Formal analysis, Data curation, Conceptualization.

Declaration of competing interest

The authors declare that they have no known competing financial interests or personal relationships that could have appeared to influence the work reported in this paper.

Acknowledgements

This work was supported by the Department of Energy (DOE), Office of Electricity (OE) at Oak Ridge National Laboratory managed by UT-Battelle LLC under contract DE-AC05-00OR22725. The employee owns all right, title and interest in and to the article and is solely responsible for its contents. The United States Government retains and the publisher, by accepting the article for publication, acknowledges that the United States Government retains a non-exclusive, paid-up, irrevocable, world-wide license to publish or reproduce the published form of this article or allow others to do so, for United States Government purposes. The DOE will provide public access to these results of federally sponsored research in accordance with the DOE Public Access Plan <https://www.energy.gov/downloads/doe-public-access-plan>. K. Hartono and R. Mallela were supported in part by the U.S. Department of Energy, Office of Science, Office of Workforce Development for Teachers and Scientists (WDTS) under the Science Undergraduate Laboratory Internships Program (SULI). Y. Ko was supported by the Graduate Research Opportunity (GRO) program managed by the Oak Ridge Institute for Science and Education (ORISE).

Data availability

Data will be made available on request.

References

- [1] Y. Nishi, Past, present and future of lithium-ion batteries: can new technologies open up new horizons?, in: *Lithium-ion Batteries* Elsevier, 2014, pp. 21–39.
- [2] N. Mao, et al., A comparative analysis of lithium-ion batteries with different cathodes under overheating and nail penetration conditions, *Energy* 278 (2023).
- [3] Y.S. Tian, et al., Promises and challenges of next-generation “beyond li-ion” batteries for electric vehicles and grid decarbonization, *Chem. Rev.* 121 (3) (2021) 1623–1669.
- [4] P.J. Bugryniec, et al., Review of gas emissions from lithium-ion battery thermal runaway failure - considering toxic and flammable compounds, *J. Energy Storage* (2024) 87.
- [5] Y.Q. Chen, et al., A review of lithium-ion battery safety concerns: the issues, strategies, and testing standards, *J. Energy Chem.* 59 (2021) 83–99.
- [6] X.Y. Hu, et al., Experimental study on the thermal runaway hazard quantification and its assessment parameters in the lithium-ion battery, *J. Energy Storage* (2024) 101.
- [7] A. García, et al., Analysis of the thermal runaway phenomenon of nickel-manganese-cobalt cells induced by nail penetration through high-speed infrared imaging, *J. Energy Storage* (2024) 75.
- [8] L. Lin, et al., Mechanically induced thermal runaway severity analysis for Li-ion batteries, *J. Energy Storage* (2023) 61.
- [9] European Council for Automotive R&D, *Battery Requirements for Future Automotive Applications*, 2019.
- [10] L.S. Lin, et al., Dataset of mechanically induced thermal runaway measurement and severity level on Li-ion batteries, *Data Brief* (2024) 55.
- [11] Sandia National Laboratories Grid Energy Storage Department, *Battery archive*, Available from: <https://batteryarchive.org/index.html>, 2019 (11/18/2024).
- [12] Z.X. Zeng, et al., Study on the thermal runaway behavior and mechanism of 18650 lithium-ion battery induced by external short circuit, *Appl. Therm. Eng.* 258 (2025).
- [13] J.Y. Chen, et al., The thermal-gas coupling mechanism of lithium iron phosphate batteries during thermal runaway, *J. Power Sources* 625 (2025).
- [14] G. Zhou, et al., Experimental study on the thermal runaway and flame dynamics of NCM811 lithium-ion batteries with critical thermal load under variable penetration condition, *Int. Commun. Heat Mass Transf.* 158 (2024).
- [15] K. Wang, et al., Thermal runaway evolution of a 4S4P lithium-ion battery pack induced by both overcharging and unilateral preheating, *Case Stud. Therm. Eng.* (2024) 63.
- [16] J.F. Wang, et al., A comparative study of overcharge thermal runaway force-electrical-thermal characteristics and safety assessment of lithium batteries with different cathode materials, *Appl. Therm. Eng.* 256 (2024).
- [17] B.S. Nie, Y.S. Dong, L. Chang, The evolution of thermal runaway parameters of lithium-ion batteries under different abuse conditions: a review, *J. Energy Storage* (2024) 96.
- [18] A.V. Shelke, et al., Characterizing and predicting 21700 NMC lithium-ion battery thermal runaway induced by nail penetration, *Appl. Therm. Eng.* 209 (2022).
- [19] T. Yokoshima, et al., Direct observation of internal state of thermal runaway in lithium ion battery during nail-penetration test, *J. Power Sources* 393 (2018) 67–74.
- [20] W. Ke, et al., Experimental study on the characteristics of thermal runaway propagation process of cylindrical lithium-ion batteries, *Energy Sources A Recover. Util. Environ. Effects* 46 (1) (2024) 11379–11394.
- [21] N. Kafadarova, et al., A system for determining the surface temperature of cylindrical lithium-ion batteries using a thermal imaging camera, *Batteries-Basel* 9 (10) (2023).
- [22] S.X. Zhu, et al., A novel designed visualized Li-ion battery for in-situ measuring the variation of internal temperature, *Extreme Mech. Lett.* (2020) 37.
- [23] J. Bohse, Acoustic emission examination of polymer-matrix composites, *J. Acoust. Emission* 22 (2004) 208–223.
- [24] A. Huijzer, C. Kassapoglou, L. Phalavan, Acoustic emission monitoring of carbon fibre reinforced composites with embedded sensors for in-situ damage identification, *Sensors* 21 (20) (2021).
- [25] S. Schweidler, et al., The sound of batteries: an operando acoustic emission study of the LiNiO₂ cathode in Li-ion cells, *Batter. Supercaps* 3 (10) (2020) 1021–1027.
- [26] T. Ohzuku, N. Matoba, K. Sawai, Direct evidence on anomalous expansion of graphite-negative electrodes on first charge by dilatometry, *J. Power Sources* 97–8 (2001) 73–77.
- [27] N. Kircheva, et al., Study of solid electrolyte interface formation and lithium intercalation in Li-ion batteries by acoustic emission, *J. Electrochem. Soc.* 159 (1) (2012) A18–A25.
- [28] K. Rhodes, et al., Understanding the degradation of silicon electrodes for lithium-ion batteries using acoustic emission, *J. Electrochem. Soc.* 157 (12) (2010) A1354–A1360.
- [29] C.Y. Choe, W.S. Jung, J.W. Byeon, Damage evaluation in lithium cobalt oxide/carbon electrodes of secondary battery by acoustic emission monitoring, *Mater. Trans.* 56 (2) (2015) 269–273.
- [30] W.F. Hao, et al., Damage analysis of cylindrical lithium-ion cells under three-points bending using acoustic emission, *J. Power Sources* 444 (2019).
- [31] S. Schweidler, et al., Acoustic emission monitoring of degradation processes in lithium-ion batteries with a high-entropy oxide anode, *Sci. Rep.* 11 (1) (2021).
- [32] Z.X. Huang, et al., Failure mechanisms and acoustic responses of cylindrical lithium-ion batteries under compression loadings, *Eng. Fail. Anal.* 163 (2024).
- [33] W.F. Hao, et al., Study on mechanical properties and failure mechanism of 18650 Lithium-ion battery using digital image correlation and acoustic emission, *J. Energy Storage* (2021) 41.
- [34] Y. Samantaray, et al., Electrochemically resolved acoustic emissions from li-ion batteries, in: *M.I.o. Technology* (Ed.), ChemRxiv, 2025.
- [35] Battery archive, Available from: [www.batteryarchive.org](https://batteryarchive.org) (cited 2025 March 17).
- [36] Vallen Systeme GmbH, *AMSY-6 System Description - System Description*, 2021.
- [37] D. Brace, *The Laws of Radiation and Absorption*, American Book Company, 1901.
- [38] X. Zhang, et al., A critical review of thermal runaway prediction and early-warning methods for lithium-ion batteries, *Energy Mater. Adv.* (2023) 4.
- [39] R. Zhao, J. Liu, J.J. Gu, Simulation and experimental study on lithium ion battery short circuit, *Appl. Energy* 173 (2016) 29–39.
- [40] N.E. Galushkin, N.N. Yazvinskaya, D.N. Galushkin, Mechanism of thermal runaway in lithium-ion cells, *J. Electrochem. Soc.* 165 (7) (2018) A1303–A1308.
- [41] Q.S. Wang, et al., Thermal runaway caused fire and explosion of lithium ion battery, *J. Power Sources* 208 (2012) 210–224.
- [42] Y.X. Dai, A. Panahi, Thermal runaway process in lithium-ion batteries: a review, *Next Energy* (2025) 6.